JGR Planets

RESEARCH ARTICLE

10.1029/2024JE008888

Dust Lifting and Deposition Over Six Mars Years at Gale Crater, Mars, From REMS Observations and Mesoscale Simulations

A. Vicente-Retortillo[1], G. M. Martinez[1], C. E. Newman[2], M. T. Lemmon[3], J. R. Johnson[4], E. L. Mason[5], N. O. Renno[6], and J. A. Rodriguez-Manfredi[1]

[1]Centro de Astrobiologia (INTA-CSIC), Madrid, Spain, [2]Aeolis Research, Chandler, AZ, USA, [3]Space Science Institute, Boulder, CO, USA, [4]Johns Hopkins University Applied Physics Laboratory, Laurel, MD, USA, [5]Northern Arizona University, Flagstaff, AZ, USA, [6]University of Michigan, Ann Arbor, MI, USA

Key Points:

- We show the seasonal and interannual variability of dust accumulation during six Mars Years at Gale crater, Mars
- Mesoscale simulations of dust devils and winds, and pressure drop and opacity observations, improve our understanding of dust lifting
- Dust accumulation follows similar trends on horizontal and tilted surfaces, except during the 2018 Global Dust Storm

Correspondence to:

A. Vicente-Retortillo,
adevicente@cab.inta-csic.es

Citation:

Vicente-Retortillo, A., Martinez, G. M., Newman, C. E., Lemmon, M. T., Johnson, J. R., Mason, E. L., et al. (2025). Dust lifting and deposition over six Mars Years at Gale Crater, Mars, from REMS observations and mesoscale simulations. *Journal of Geophysical Research: Planets*, *130*, e2024JE008888. https://doi.org/10.1029/2024JE008888

Received 4 DEC 2024
Accepted 2 MAY 2025

© 2025. The Author(s).
This is an open access article under the terms of the Creative Commons Attribution-NonCommercial-NoDerivs License, which permits use and distribution in any medium, provided the original work is properly cited, the use is non-commercial and no modifications or adaptations are made.

Abstract We present the temporal evolution of the effect of dust accumulation on two surfaces of the Curiosity rover at Gale crater during almost 4,000 sols using Rover Environmental Monitoring Station (REMS), Chemcam and Mastcam observations, and compare it with simulations of the Mars Weather Research and Forecasting Model (MarsWRF) atmospheric numerical model and environmental observations to improve our understanding of dust lifting on Mars. After almost six full Mars Years (MY), dust accumulated on the REMS UV sensor (UVS) attenuates an average of 45% of the incoming radiation. Dust accumulation on the UVS follows a seasonal cycle with gradual dust accumulation during the aphelion season followed by dust removal until $L_s \sim 300°$. However, there is a strong interannual variability during the dusty season. MarsWRF simulations show that wind stress has a strong diurnal, seasonal and interannual variability; simulations of dust devil activity show a seasonal pattern that aligns with pressure drop observations, peaking also at $L_s \sim 300°$. Dust lifting mechanisms are variable, with a larger relative importance of wind stress in MY 31 and 32, and of dust devils in MY 34 to 36. Dust accumulation on the Chemcam calibration target follows a very similar temporal evolution, but with a marked offset since the 2018 Global Dust Storm, suggesting that surface tilt is particularly important around intense dust storms. We characterize dust lifting mechanisms at Gale crater and quantify the effect of dust accumulation during an extraordinary dust storm on different surfaces; the observed net removal periods validate MarsWRF simulations and suggest the suitability of Gale Crater for long-term solar-powered missions.

Plain Language Summary The Martian dust cycle governs the modern martian environment and affects surface missions. We present the evolution of dust accumulation on the Curiosity rover during more than 11 Earth years and compare it with environmental observations and simulations, improving our understanding of dust lifting on Mars. After 11 years, dust attenuates less than half of the incoming radiation, indicating the suitability of the Gale crater for future solar-powered missions. Dust accumulation follows a seasonal cycle, presenting a minimum during local Summer, with gradual accumulation during the non-dusty season. Winds present strong diurnal, seasonal and interannual variability, while dust devil activity presents a relatively repeatable seasonal pattern with a maximum in Summer. Periods of dust removal and minimum dust accumulation align with periods of strong winds early in the mission and with the dust devil activity cycle in more recent years. Dust accumulation on a tilted surface follows very similar trends except during the global dust storm in 2018. We have characterized dust lifting at the Gale crater and quantified the effect of dust accumulation on different surfaces, including the changes caused by an extraordinary dust storm.

1. Introduction

The Martian dust cycle governs the modern martian environment and strongly affects surface missions. Dust is lofted by convective vortices (i.e., dust devils) and by surface wind stresses, forming dust clouds or hazes that can range from local events to global dust storms (Kahre et al., 2017, and references therein). The characterization of these dust lifting mechanisms is necessary to improve our understanding and representation of the Martian atmospheric dynamics and climate, and a wide number of efforts have been carried out with General Circulation Models (Basu et al., 2004; Kahre et al., 2006; Newman et al., 2002a, 2002b), and mesoscale and large-eddy simulation modeling (Michaels, 2006; Newman et al., 2017, 2019; Rafkin et al., 2001; Spiga & Forget, 2009; Spiga et al., 2013, 2021). After being lofted, dust is transported and deposited on the surface. Dust accumulation



Figure 1. Combined Mastcam product showing the location of the REMS UV Sensor (UVS) and the ChemCam Calibration Target (CCCT). A zoom of the CCCT showing the location of Target #11 is shown in the upper right corner. The product corresponds to sol 2,137 of the MSL mission and includes parts of mcam011460 and mcam011461. Image credit: NASA/JPL-Caltech/MSSS.

has a negative impact on surface hardware and degrades or damages instrumentation; this effect is particularly critical for solar-powered missions, where dust accumulation on the solar panels limits energy production and can lead to the premature end of the mission. Since solar power has been identified as the most practical solution for future reduced-cost missions (MEPAG MCE-SAG, 2023), the knowledge of the temporal evolution of dust accumulation becomes critical.

The Mars Science Laboratory (MSL) Curiosity rover (Grotzinger et al., 2012) landed at Gale crater (4.6°S, 137.4°E) in 2012, carrying scientific instruments that allow characterizing the effect of dust accumulation on surfaces with different tilts and the occurrence of dust lifting events of various intensities. In this study, we will combine measurements from three instruments: The Rover Environmental Monitoring Station (REMS), the Mast camera (Mastcam) and the Chemistry and Camera (ChemCam) spectrometers. REMS (Gómez-Elvira et al., 2012) is comprised of sensors that measure UV radiation, pressure, surface and air temperatures, relative humidity and wind speed. The REMS UV Sensor (UVS) is mounted horizontally on the rover deck (Figure 1), being therefore exposed to dust deposition and removal processes, and the photocurrents provide information on the effect of dust accumulated on the sensor. The ChemCam instrument suite comprises several instruments including spectrometers and calibration targets (Wiens et al., 2012). The ChemCam calibration target (CCCT) is located on the back of the rover at an angle of 37.9° from the vertical (Figure 1); in this case, the dust cover can be analyzed from the

shape of the spectral radiances of the CCCT observations (Johnson et al., 2015). Mastcam (Bell et al., 2017) observations allow decoupling the attenuation caused by the dust accumulated on the REMS UVS from that of the dust suspended in the atmosphere.

Dust accumulation has been typically inferred from the analysis of solar panel currents. The first analysis of this type was performed from measurements during Pathfinder's 83 sols on Mars (Crisp et al., 2004). Drube et al. (2010) performed a similar analysis using measurements from the 151 sols of the Phoenix mission on Mars; they found net dust removal after sol 100, which was linked to a higher frequency of convective vortices (Ellehoj et al., 2010). The studies at the Phoenix location combined observations of dust accumulation and dust lifting processes, but the short duration of the mission did not allow the study of full seasonal variability. On the other hand, the Mars Exploration Rovers allowed the first long-term study of dust accumulation on surface assets (Stella & Herman, 2010), but the lack of an environmental suite prevented a combined analysis with data from pressure drops. Lorenz et al. (2021) present similarities and differences in dust accumulation for different missions from Pathfinder to InSight.

MSL observations have allowed the study of dust accumulation on the REMS UVS during the first 2,003 sols (Vicente-Retortillo et al., 2020) and on the Mars Hand Lens Imager (MAHLI) calibration target during the first 2,248 sols (Yingst et al., 2020). However, those analyses did not explicitly explore the variability of dust lifting mechanisms. On the other hand, dust lifting processes have been documented in detail from observations (Guzewich et al., 2023; Lemmon et al., 2017) and simulations (Newman et al., 2017, 2019; Pla-Garcia et al., 2016) but have not yet been compared with the evolution of dust accumulation. The first long-term combined analysis of the temporal evolution of dust accumulation with observations and mesoscale simulations of dust lifting mechanisms was presented in Vicente-Retortillo et al. (2018), based on the first 1,648 sols of the mission.

The current study significantly extends the temporal window of Vicente-Retortillo et al. (2018), covering now 3,953 sols. This has immediate advantages, such as a more complete characterization of the seasonal and interannual variability of dust accumulation. Moreover, it allows addressing questions that could not be covered in the aforementioned study. First, this study covers the 2018 Global Dust Storm (Guzewich et al., 2019), quantifying the effect of extraordinarily high amounts of suspended and subsequently deposited dust on rover hardware. Second, we have now used the Mars Weather Research and Forecasting Model (MarsWRF) atmospheric numerical model to perform mesoscale simulations of wind stresses and Dust Devil Activity (DDA) eight times per sol instead of one, resulting in a more comprehensive analysis. Third, we now intercompare dust accumulation on the six channels of the REMS UVS, which addresses the spatial variability in the distribution of accumulated dust. Fourth, we include results of dust cover on the CCCT, which allows comparing dust accumulation on different types of surfaces: horizontal versus tilted surfaces, with and without magnets in their proximities.

The paper is structured as follows: In Section 2, we describe the MSL instruments and observations used in this work, the methodology to calculate the effect of dust accumulation, and the MarsWRF specifications for this study. In Section 3, we present the temporal evolution of dust accumulation on the REMS UV sensor and compare it with environmental observations. In Section 4, we discuss the role of dust lifting mechanisms, the predictive skill of different wind stress and DDA thresholds for net dust removal, and the effect of surface features on dust removal and accumulation. Finally, in Section 5, we present the main conclusions of this work.

2. Data and Methodology

2.1. Mars Science Laboratory Observations

In this study, we use observations acquired by three MSL instruments: REMS, Mastcam and Chemcam. REMS is a meteorological suite that includes sensors to measure UV radiation, pressure, air and ground temperature, relative humidity and wind speed (Gómez-Elvira et al., 2012). In this study, we use UV and pressure data. REMS measurement acquisition strategy consists of nominal observation sessions of 5 min at 1 Hz at the beginning of each hour; some of those sessions are replaced by extended blocks, also at 1 Hz, which last one or more hours (Gómez-Elvira et al., 2014). The distribution of these extended blocks varies, aiming to cover all times of a sol with measurements at 1 Hz within every few sols.

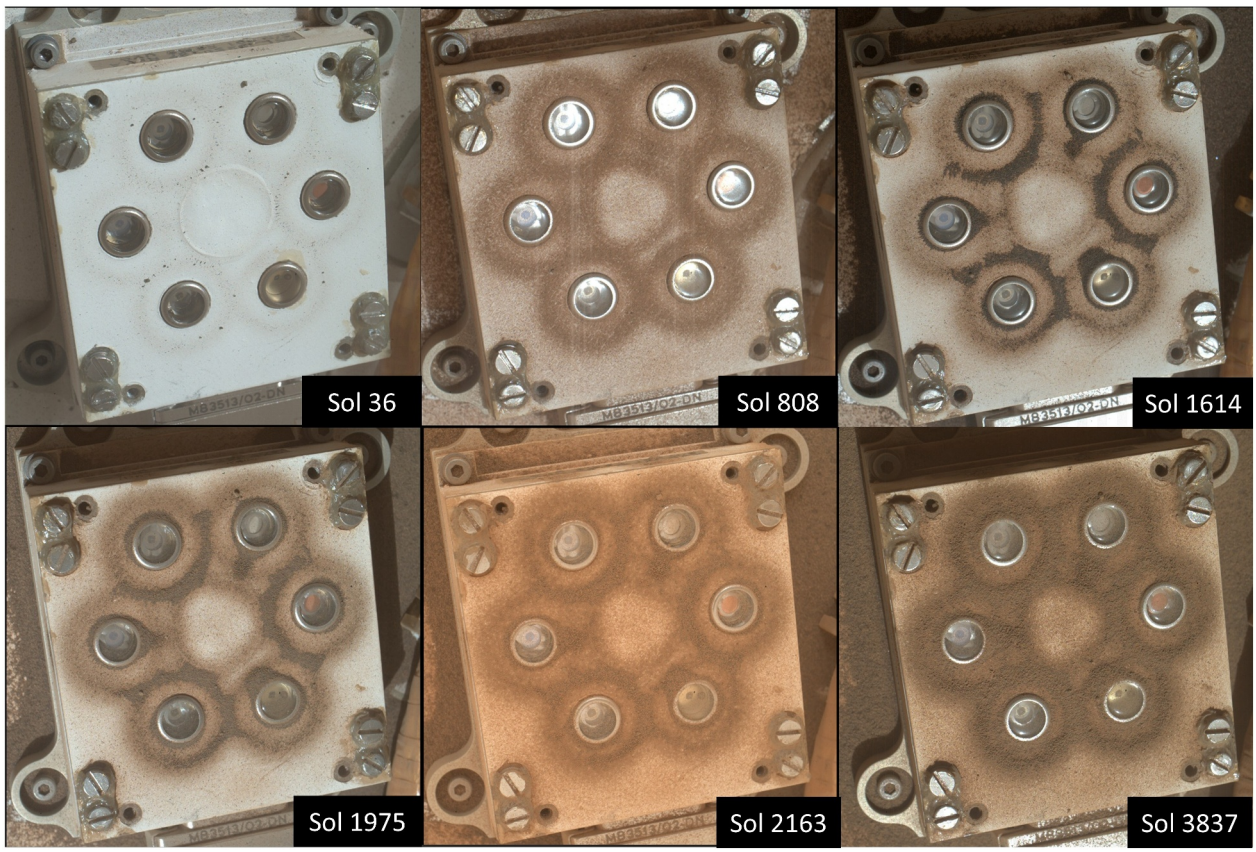


Figure 2. MAHLI images of the REMS UV sensor acquired throughout the mission showed visual evidence of dust accumulation, particularly on the magnetic rings that surround each photodiode. Net dust removal occurs between sols 808 and 1,614.

The REMS UV sensor is comprised of six photodiodes that measure at different UV wavelengths, named UVA, UVB, UVC, UVD, UVE, and UVABC (Gómez-Elvira et al., 2012). The wavelengths of peak responsivity and the full widths at half maximum (FWHM) are 340 and 32 nm for UVA, 305 and 39 nm for UVB, 260 and 39 nm for UVC, 260 and 34 nm for UVD, 330 and 27 nm for UVE, and 290 and 98 nm for UVABC (Vicente-Retortillo et al., 2020). Each photodiode is surrounded by a circular samarium cobalt magnetic ring to mitigate dust deposition on its windows (see Figures 1 and 2), similar to that on the Magnetic Properties Experiment of the Mars Exploration Rovers (Madsen et al., 2003). UV measurements are also affected by the presence of rover elements in the field of view, particularly the rover mast and masthead (Vicente-Retortillo et al., 2017), and by the motion of the robotic arm. The methodology to retrieve the effect of dust accumulation on the UVS will be described Section 2.2.

The pressure sensor is located on the rover body, and has a maximum resolution of 0.2 Pa with a time response of 1 s (Gómez-Elvira et al., 2014). Pressure measurements occasionally show small drops when rover elements cast shadows on the UVS area (Harri et al., 2014). However, this has little effect on the analysis of pressure drops inferred to be from dust lifting mechanisms (Kahanpää et al., 2016; Steakley & Murphy, 2016). Pressure drops are identified and characterized following the methodology described in Ordonez-Etxeberria et al. (2018), which we summarize next. Pressure observations are analyzed with a 60-s moving window; within this window, we perform a linear fit using the measurements during the first and last 15 s; then, we calculate the difference between the central point of the window and the linear fit at that point; if the difference exceeds 0.5 Pa, a pressure drop is identified. Some of the identified drops could be false detections, motivated by rover activities (Ordonez-Etxeberria et al., 2018), or by temporal variations in the noise of the sensor (Newman et al., 2019). Newman et al. (2019) concluded that the seasonal variability of pressure drop frequency was very similar using two methodologies. In order to avoid the effect of a variable number of observations per sol, we only consider the detections during the first 5 min of each hour.

In order to accurately calculate the effect of accumulated dust, it is necessary to know the effect of dust suspended in the Martian atmosphere. The Mast Camera (Mastcam) instrument consists of a pair of CCD cameras that can acquire multispectral images of the Martian surface and atmosphere (Bell et al., 2017), which are located in the rover masthead. Two of the filters include a 10^{-5} neutral density coating for solar images; these filters have effective wavelengths of 440 and 880 nm. Here, we use the opacities retrieved from the 880 nm images calculated following Lemmon et al. (2024a).

Finally, a comparison of dust accumulation on other rover surfaces is performed using Chemcam (Wiens et al., 2012) observations of the ChemCam calibration target (CCCT). The CCCT is comprised of 10 calibration standards, and a portion of the target holder coating is referred to as Target #11 (Johnson et al., 2015; Wiens et al., 2012). Target #11 is an effective calibration standard due to its high and relatively flat reflectance. In particular, we use radiance observations performed by the spectrometers of the ChemCam instrument in passive mode. From the passive spectra, the 535 nm band depth was calculated (Johnson et al., 2015). This band depth is sensitive to the presence of ferric oxides, and can be used as a proxy for dust cover (Johnson et al., 2015; Morris et al., 2000; Rice et al., 2022).

2.2. Calculation of the Dust Correction Factor

We quantify the effect of dust accumulation on the REMS UVS by means of a Dust Correction Factor (DCF). The DCF represents the fraction of the incoming radiation that reaches the photodiode through the dust accumulated on the window (as an example, 1 represents a clean surface, and 0.6 indicates that accumulated dust causes an additional attenuation of 40%). The methodology to calculate the DCF is described in Vicente-Retortillo et al. (2018) and Vicente-Retortillo et al. (2020), with some minor improvements. Next, we summarize the main steps of our analysis and describe the modification from previous analyses (inclusion of the fifth step described below).

The first step of the analysis consists of discarding measurements that could be affected by the presence of rover elements in the field of view or by rover operation activities. This is performed by analyzing and filtering the ancillary data, which can be found in the NASA PDS as REMS ADR files. Specifically, we discard measurements in which the solar azimuth angle with respect to the rover is between $-10°$ and $100°$ (the quadrant of the field of view which is partially blocked by the rover mast and masthead and an additional margin), those when the masthead was not in the most typical position, and those during rover or arm motion.

Second, we organize the photodiode output currents, available in the NASA PDS as TELRDR files, as a function of sol number and Sun position relative to the REMS UV sensor. We use the photocurrents (in nA) instead of the fluxes (in W/m^2) due to inaccuracies in the angular response functions that were used to generate the processed ENVRDR and MODRDR PDS files (Vicente-Retortillo et al., 2020).

Third, we apply a conversion factor to the measurements. This factor is obtained with the radiative transfer model COMIMART (Vicente-Retortillo et al., 2015), and considers the atmospheric opacity (measured by Mastcam), the Sun–Mars distance, the solar zenith angle, the wavelength range, and the rover tilt and orientation (available in the ancillary ADR files).

Fourth, for each pair of sols with available opacity measurements and with measurements with similar solar position, we calculate a relative DCF by dividing the corresponding photocurrents obtained in the previous step. If there are measurements on both sols for more than one solar position, we use the one with the highest sum of the photocurrents. Then, we normalize all the relative DCF that were calculated using a given sol as a reference, and this process is repeated for every sol with mastcam opacity measurements.

The fifth step of the analysis is the application of an automatic outlier detection algorithm; this is an improvement with respect to previous versions. We first calculate a smoothed version of the DCF for each channel by using a triangular weighting function to values within 50 sols of each sol (individual DCF values are multiplied by 50 minus the number of sols to the center of the averaging window and their sum is divided by the sum of the weights). Then, we calculate the differences between the smoothed and individual values for each sol. If differences are above a given threshold or if there are large differences among channels, then the individual value for that sol is identified as an outlier and removed from the temporal series. Finally, in the last step, for consistency with previous studies (Smith et al., 2016; Vicente-Retortillo et al., 2018, 2020), the filtered individual values are smoothed using the same triangular weighting function.

2.3. MarsWRF Simulations

MarsWRF is based on the terrestrial Weather Research and Forecasting (WRF) model, adapted to Mars (Richardson et al., 2007). The model has a global domain with five embedded domains with decreasing coverage and increasing resolution; the innermost domain covers the region of the Curiosity rover traverse and has a horizontal resolution of ∼490 m (Newman et al., 2017).

Dust lifting is parametrized through near-surface wind stress and dust devil activity. Wind stress is obtained from the product of the atmospheric density and the squared drag velocity, which is in turn obtained from the total wind speed at the lowest prognostic level (Garratt, 1994; Newman et al., 2002a, 2017).

Dust devils are treated in MarsWRF as convective heat engines. Rennó et al. (1998) presented a comprehensive thermodynamic theory in which the Dust Devil Activity (the flux of energy available to drive the vortices, DDA) is proportional to the boundary layer thickness and the sensible heat flux. In MarsWRF, the sensible heat flux depends on air density, drag velocity and the difference between surface and near-surface temperatures (Newman et al., 2019).

3. Results

3.1. Dust Accumulation on the REMS UV Sensor

In this section, we analyze the temporal evolution and the spatial distribution of dust accumulation on the REMS UV Sensor. The assessment of the spatial distribution of the accumulated dust can be first performed by analyzing the images of the REMS UV Sensor that are acquired periodically by the MAHLI instrument.

MAHLI has acquired 60 images of the REMS UV Sensor during the first 3,953 sols of the mission. Figure 2 shows a selection of them, corresponding to sols 36, 808, 1,614, 1,975, 2,163, and 3,837. These images have been selected because they represent key moments of the mission or because visual changes become particularly clear: the image on sol 36 is the first taken, it represents the state of the sensor at the beginning of the mission, which was not completely clean; the images on sols 1,975 and 2,163 show significant dust accumulation due to the MY 34 Global Dust Storm; the images on sols 808 and 1,614 clearly illustrate net dust deposition between sols 36 and 808 and net dust removal between sols 808 and 1,614; finally, the image on sol 3,837 represents the state of the sensor close to the end of the analyzed period. These images are extremely useful to understand the spatial variability of the accumulated dust. Dust accumulation is particularly intense on the circular magnetic rings that surround each photodiode, and the images also show that the dust distribution changes with time: focusing on the circular patterns, in some images dust accumulation has a relatively homogeneous appearance (sols 808 and 3,837), but in others there are clear heterogeneities (sols 1,614 and 1,975). Although these shed light on the spatial distribution of dust, it is very difficult to perform a quantitative study using them. We will now assess the variability (temporal and spatial) of dust accumulation quantitatively by means of the DCF on the six photodiode windows obtained from REMS UV measurements.

Figure 3 shows the temporal evolution of the Dust Correction Factor during the first 3,953 sols of the MSL mission for the six channels of the REMS UV Sensor: UVA (blue), UVB (orange), UVC (yellow), UVD (purple), UVE (green) and UVABC (light blue). The DCF corroborates the qualitative analysis of the images presented in Figure 2. At the beginning of the mission, there was a period of significant net dust deposition, with dust accumulation reaching a local maximum at around sol 800. Then, the period between sols 808 and 1,614 was characterized by net dust removal, but the analysis of the DCF also shows that between these two images there were actually two strong net dust removal periods separated by a period of net dust accumulation. Then, there is another period of net dust accumulation before the acquisition of the next image (sol 1,975). The most dramatic change occurred during the peak of the GDS, when the DCF showed a steep decrease (indicating dust accumulation) until sol ∼2,120, consistent with the abundant dust cover imaged on sol 2,163. Finally, the DCF suggests that when the last image was acquired, the sensor was slightly dustier than on sol 2,163, but it also shows that between these images the sensor underwent several periods of net dust removal and deposition.

The six channels show the same temporal evolution, enhancing the confidence in the characterization of periods of net dust removal and deposition. However, there are quantitative differences among them. The effect of dust accumulation on the UVC channel is larger than on the UVB, which is in turn larger than on the UVA. The behavior of these three channels suggests that the effect of the accumulated dust could increase as the wavelength

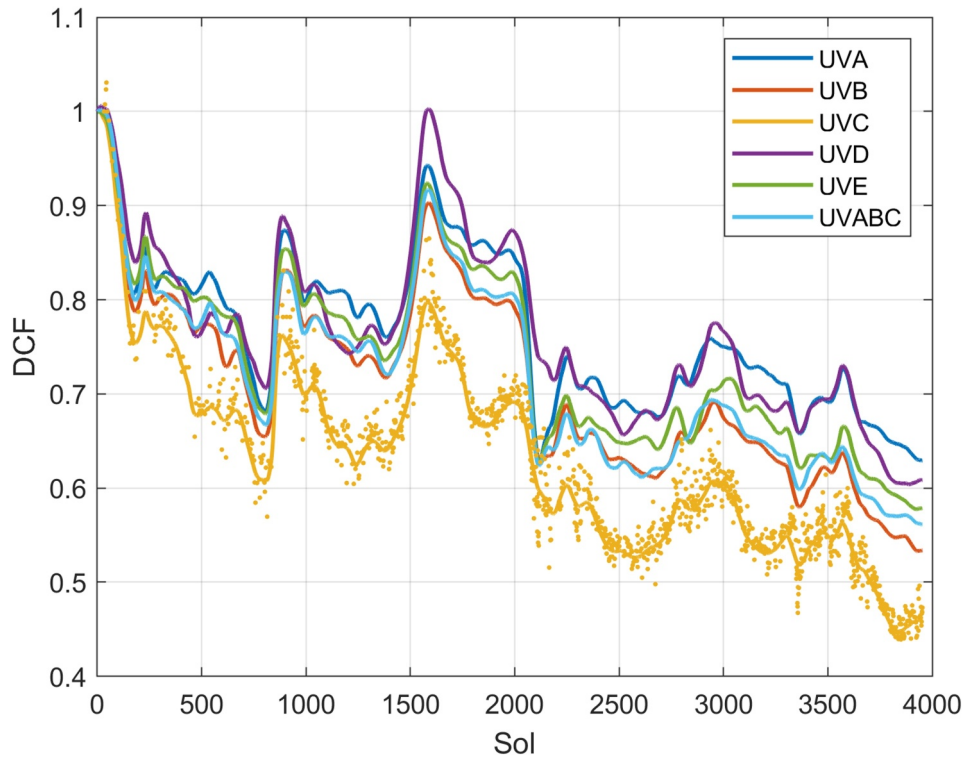


Figure 3. Temporal evolution of the Dust Correction Factor during the first 3,953 sols of the MSL mission for the six REMS UV channels. Dots indicate individual values for the UVC channel.

decreases; however, channels UVD and UVE do not follow this trend, since UVE values are lower than the UVD values, which are close to those of the UVA (and occasionally the highest). For this reason, it is more likely that the differences among channels are the combined effect of spatial heterogeneities in dust distribution (supported by the images of the REMS UVS) and measuring wavelength differences.

Dots in Figure 3 represent the individual DCF values for the UVC channel. The high sol-to-sol variability of these values is mainly attributed to noise and not to actual changes in dust coverage; this is corroborated by the relatively low correlation (R^2 between 0.57 and 0.68) of the sol-to-sol differences among pairs of channels. This high noise in individual values precludes us from a conclusive analysis of sol-to-sol variations, and therefore for the rest of the study we focus on the smoothed temporal series obtained as described in Section 2.2.

We will now analyze in greater detail the temporal evolution of accumulated dust. Figure 4 shows the DCF averaged over the six channels (the average of the six smoothed series shown in Figure 3) as a function of solar longitude (L_s) and Mars Year during the first 3,953 sols of the mission, covering almost six full Mars Years (from MY 31, $L_s \sim 150°$ to MY 37, $L_s \sim 120°$).

Figure 4 shows that the DCF follows a seasonal pattern, with a local maximum (a minimum in dust accumulation) at around $L_s = 300°$, followed by a gradual decrease until approximately the beginning of the storm season, where a period of net dust removal can be found in every year. This cycle appears counterintuitive because net dust accumulation occurs during the relatively clear season and net dust removal occurs during the dusty season. This indicates that dust removal mechanisms are active at the Gale Crater. These mechanisms are analyzed in detail in Section 4.1.

In addition to the seasonal cycle, dust accumulation shows significant interannual variability during the perihelion ($L_s = 251°$) season. MY 34 follows a particularly distinct behavior, presenting the most abrupt increase in dust accumulation at the beginning of the season; this behavior was caused by the 2018 Global Dust Storm, which presented extraordinarily high opacities ($\tau > 8$) at Gale crater (Guzewich et al., 2019), causing a decrease in UV radiation by more than 95%. Still, after the storm, there was a period of net dust removal that lasted until $L_s = 300°$ (this will be further discussed in Section 4.2). The other large decrease of the DCF was observed at the beginning

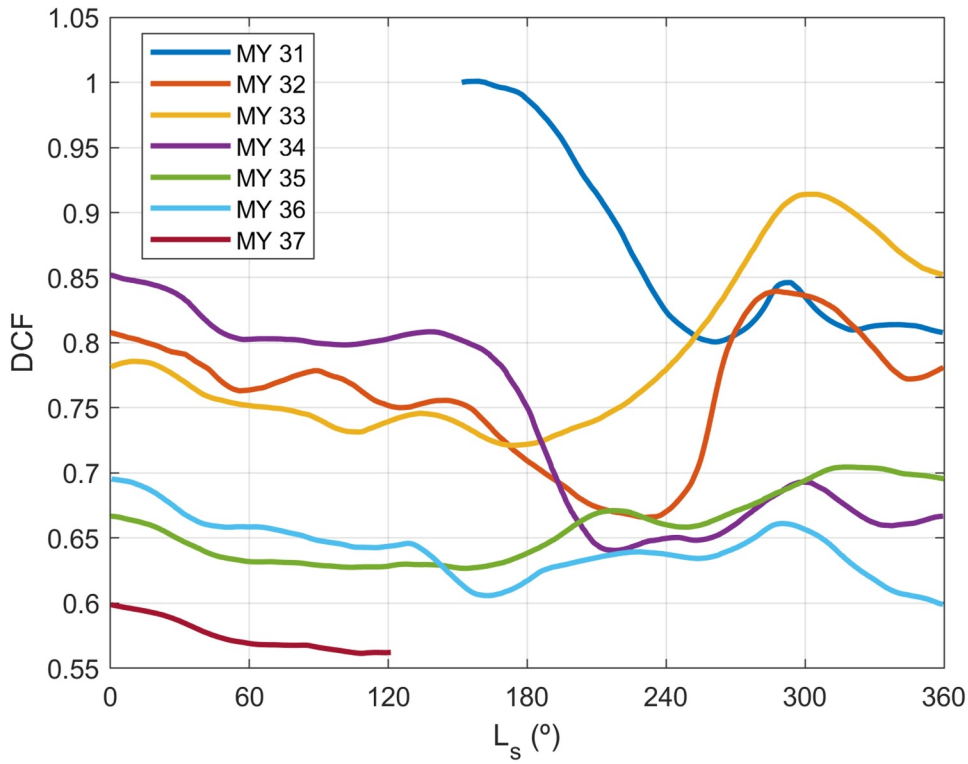


Figure 4. Averaged DCF as a function of solar longitude and Mars Year, showing seasonal and interannual variability.

of the mission (MY 31), potentially related to a low efficiency of dust removal mechanisms (see Sections 3.2 and 4.1) and to the fact that the sensor was relatively clean, minimizing the effect of dust removal and maximizing that of dust deposition. In the remaining four years, there is net dust removal but also with interannual variability: The net dust removal periods of MY 32 and MY 33 are intense, with that on MY 32 being the shortest due to a relatively late start, while those on MY 35 and MY 36 are significantly weaker. This interannual variability during the dusty season implies that the annual net effect also depends on the year: MY 31 and 34 present significant net increases in dust accumulation, MY 32 and MY 36 show slight to moderate increases, and MY 33 and MY 35 show slight to moderate decreases. In contrast, during the aphelion ($L_s = 71°$) season, there is very little interannual variability; the most remarkable difference is the period of enhanced net dust accumulation at around MY 36, $L_s = 155°$ due to an early regional dust storm (Martín-Rubio, Vicente-Retortillo, Martínez-Esteve, et al., 2024), which led to opacities at Gale of $\tau \sim 2$, which is similar or even higher than the typical annual maximum (see Figure 5).

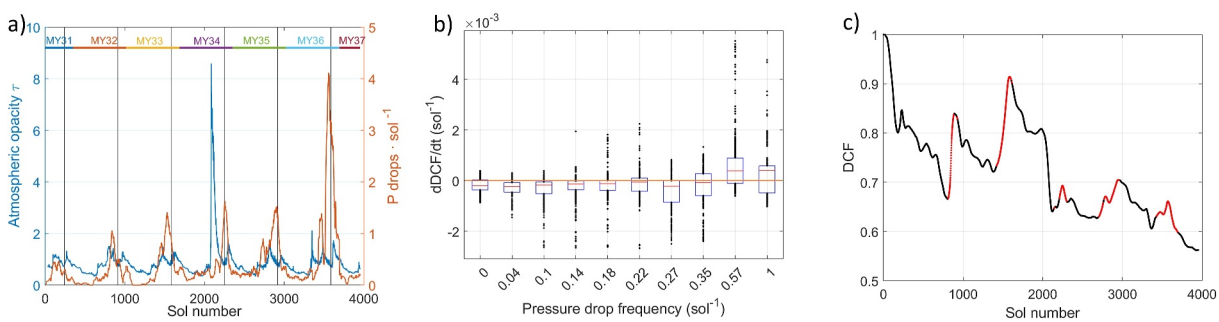


Figure 5. (a) Environmental variables measured by MSL throughout the mission: atmospheric opacity (blue) and pressure drop frequency (orange). Mars Years are shown at the top, following the color code of Figure 4. Vertical lines correspond to $L_s = 300°$; (b) Boxplot showing the time rate of the DCF change as a function of the observed pressure drop frequency; the orange line separates net dust removal from net dust accumulation; (c) DCF, with values during periods of high pressure drop frequency highlighted in red.

The DCF for MSL can be compared to that of other missions at other locations. For this comparison we select missions with a duration above one Mars Year (Mars Exploration Rovers Spirit and Opportunity, InSight Lander and Mars 2020 Perseverance Rover); to remove the effect of seasonality, we perform the comparison after a given number of full Mars Years (three for Spirit and Opportunity, and one for InSight and Mars 2020). DCF values for other missions have been obtained from Lorenz et al. (2021) except for Mars 2020, which were presented in Vicente-Retortillo et al. (2024). After three Mars Years, the DCF for Spirit and Opportunity were around 0.78 and 0.60, respectively, lower than the value of 0.80 observed by MSL; the value for Spirit appears similar, but it is preceded by a strong dust removal event, and the DCF was below 0.30 around sol 1,800; on average, the DCF for Spirit during the first 3 Mars Years was 0.60, clearly below the mean DCF of 0.80 observed by MSL. The DCF for Mars 2020 was reduced by 20% during the first Mars Year, which is similar to the 25% reduction for MSL. Finally, the DCF for InSight after one Mars Year was 0.27, clearly lower than the value for MSL (0.75). In summary, the effect of dust accumulation for MSL is lower than for the majority of the previous long-term missions, and the total attenuation of 45% after almost six full Mars Years highlights the suitability of Gale crater for long-term solar-powered missions.

3.2. Comparison With MSL Environmental Observations

The behavior of dust accumulation, showing periods of net dust removal, suggests that dust lifting mechanisms play an important role at the Gale Crater. Following Vicente-Retortillo et al. (2018), we will first analyze the behavior of the DCF by comparing it with environmental variables measured by MSL instruments. In particular, we will compare the results with two relevant values: first, dust opacity, which indicates the abundance of dust in the atmosphere and that could potentially be deposited on the surface; and second, pressure drop frequency, which is related to the likelihood of dust lifting mechanisms.

Figure 5a shows the temporal evolution of the measured environmental variables that are related to dust lifting and deposition. The dust opacity (blue line) follows a seasonal cycle, with typically two local maxima per year (Lemmon et al., 2024a; Martinez et al., 2017), which correspond to the occurrence of regional dust storms (Kass et al., 2016; Martín-Rubio, Vicente-Retortillo, Gómez, & Rodríguez-Manfredi, 2024). The peak showing atmospheric opacity values above 8 corresponds to the 2018 Global Dust Storm, which had a strong impact at the Gale crater (Guzewich et al., 2019). The pressure drop frequency also shows a seasonal cycle, which peaks during the perihelion season (typically between the two periods of enhanced opacity, roughly around $L_s = 300°$) and low values during the low opacity season. Pressure drop frequency is particularly high around intense bursts of turbulent activity linked to local and regional winds, which occur at night around the perihelion at specific locations that favor turbulence (Newman et al., 2019; Ordonez-Etxeberria et al., 2018). On the other hand, previous studies of pressure drops have identified false detections that correspond to spurious drops caused by rover activities, which show a homogeneous temporal distribution (Ordonez-Etxeberria et al., 2018), or to an increase in instrument noise, more noticeable in interannual scales (Newman et al., 2019). Hence, the large peak in MY 36 appears to be the result of frequent nighttime bursts of activity, but it could also be affected by a larger fraction of false detections during this year. Since our interest is focused on the timing of the annual maximum pressure drop frequency, the effect of considering false detections is minimized since they do not alter the seasonal cycle.

Figure 5b shows the time rate of DCF change as a function of pressure drop frequency. The values of the horizontal axis correspond to the deciles of the pressure drop frequency (from minimum to the 9th decile), so that the 10 distributions presented in this figure contain subsets of the same size, favoring the comparison. The first eight distributions, which correspond to the entire data set except for the 20% of the highest pressure drop frequencies, are very similar to each other, with a marked predominance of negative values (indicating net dust accumulation). In contrast, the last two distributions show a clearly distinct behavior, concentrating most of the positive values (representing net dust removal). Hence, the results indicate that when the number of detected pressure drops during the first 5 min of each hour exceeds approximately one every two sols, net dust removal is expected.

To corroborate this link between pressure drop frequency and dust removal, Figure 5c shows the DCF in black, and the values with the highest pressure drop frequency (above 80th percentile) are highlighted in red. The periods of high pressure drop frequency align with those of net dust removal, particularly during MY 32, MY 33, and MY 35, and with the annual maxima (representing annual minima of dust accumulation), particularly in MY 34 and MY 36. Hence, during the period of high pressure drop frequency, even though the opacities are relatively high, dust lifting mechanisms remove more dust than what is deposited. Similarly, even though the opacities are low,

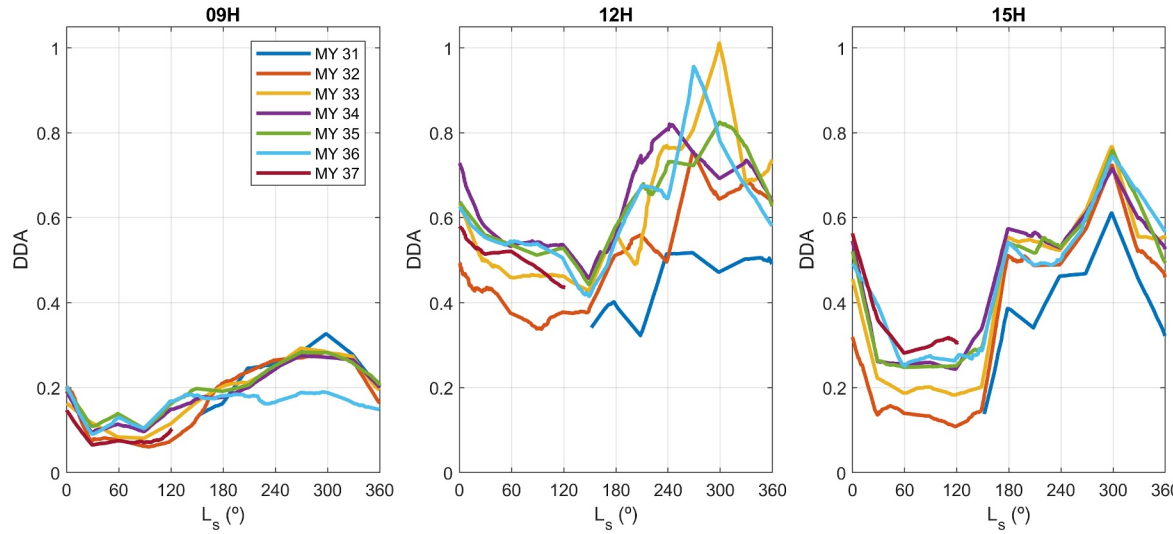


Figure 6. Seasonal and interannual variability of Dust Devil Activity at the location of the MSL Curiosity rover, simulated with MarsWRF. Each panel corresponds to a local time indicated in the title. The corresponding Mars Year for each color is shown in the panel at 09H.

more dust is deposited than it is removed during the period of low pressure drop frequency. The strong increase in dust accumulation slightly after sol 2,000 was caused by the Global Dust Storm, and the strong decrease at the beginning of the mission could be a combination of high opacities and relatively low pressure drop frequency. In Section 4, we will further analyze the predictive skill of different thresholds for net dust removal relying on the observed pressure drop frequency.

4. Discussion

4.1. Dust Lifting Mechanisms and Dust Removal Thresholds

The results of the previous section can be complemented with the analysis of MarsWRF simulations of dust devil activity and wind stress. Dust lifting could be caused by dust devils or by wind gusts. REMS also includes a wind sensor but partially fails after landing, limiting notably the amount of available measurements (Newman et al., 2017), and the sensor completely fails around sol 1,500 (Viudez-Moreiras et al., 2019). On the other hand, pressure drops can be attributed to both convective vortices and turbulence (Vicente-Retortillo et al., 2018), and a small fraction of them are false detections caused by various effects (Ordonez-Etxeberria et al., 2018). For these reasons, and in order to assess the intensity and variability of both dust lifting mechanisms, we have analyzed MarsWRF simulations of DDA and wind stress at 8 hr per sol during the first 3,953 sols of the mission.

Figure 6 shows the DDA as a function of solar longitude and Mars Year (colors) at three local times: 9, 12, and 15H (dust devil activity is negligible at other times; Newman et al., 2019). DDA has strong similarities to the pattern of sensible heat flux (Newman et al., 2019), which increases with the difference between surface and air temperatures, and this difference responds quickly to solar heating, peaking around noon (Martinez et al., 2021). DDA is also affected by the thermodynamic efficiency of the dust devil convective heat engine (Rennó et al., 1998), related to the depth of the Planetary Boundary Layer, which peaks a couple of hours after noon (Newman et al., 2019). Hence, values at 9H are lower because either the sensible heat flux or the thermodynamic efficiency, or both, is lower than at the other two times. Regardless of the time of the day, the DDA presents a marked seasonal cycle, peaking in local summer at around $L_s = 300°$; sensible heat flux shows little seasonal variability (Martinez et al., 2021); therefore, this seasonal cycle is mainly attributed to the variability in thermodynamic efficiency in the region of the rover traverse, although this does not apply to other regions of Gale crater (Newman et al., 2019). In general, the interannual variability is small, with the highest values found in MY 33 and MY 36, and the lowest values in MY 31.

Figure 7 shows the wind stress simulated with MarsWRF 8 times per sol (every three hours between 0 and 21H). Contrary to the DDA, wind stress presents a strong variability in all time scales: intrasol, seasonal and interannual. In general, wind stress follows a seasonal cycle that is relatively similar to that of dust devil activity, peaking

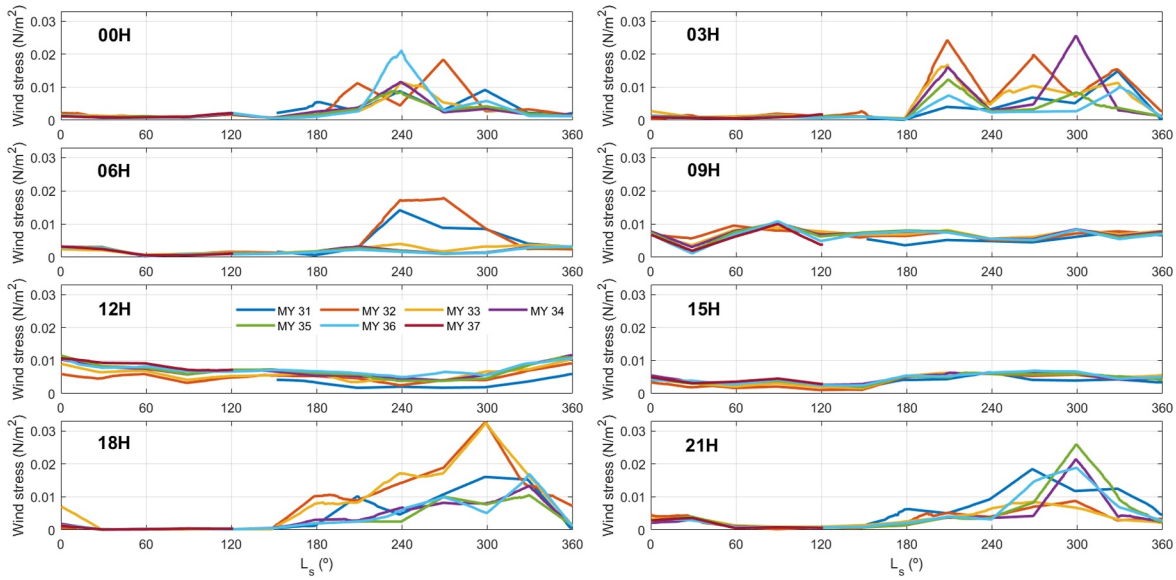


Figure 7. Seasonal and interannual variability of wind stress at the location of the MSL Curiosity rover, simulated with MarsWRF. Each panel corresponds to a local time indicated in the upper left corner. The corresponding Mars Year for each color is shown in the panel at 12H.

during the dusty perihelion season. However, the intensity of this cycle strongly depends on the local time, being clear during nighttime and very weak during daytime. The figure shows that there is a strong interannual variability; a clear example is found in the winds at 18H: their seasonal cycles in MY 32 and MY 33 are very similar, with a strong peak at $L_s = 300°$; in contrast, the cycle in the following years is markedly less intense and there are no strong peaks at $L_s = 300°$; moreover, the cycle at 21H experiences the opposite changes: the peaks corresponding to annual maxima at $L_s = 300°$ in MY 34, 35, and 36 are not present in MY 32 and 33. The interpretation of the simulations is that winds are particularly intense around local early summer (summer solstice occurs at $L_s = 270°$), when external northerly winds penetrate into the crater, influencing the local circulation (Newman et al., 2017; Rafkin et al., 2016): the external flows reinforce downslope flows that may affect the MSL location; since wind patterns are strongly affected by local topography, the changing location of the rover is the main responsible of the expected interannual variability.

We will now compare the DCF to the daily maxima of dust devil activity and wind stress. This is an update with respect to the analysis performed by Vicente-Retortillo et al. (2018), where the DCF was compared against the DDA at noon and wind stress at midnight.

Figure 8 shows the time rate of DCF change as a function of the daily maxima of wind stress (left) and DDA (right). As for the pressure drop frequency, each distribution corresponds to one decile of the corresponding variable. In the case of wind stress, the last two distributions contain most of the positive changes and all of the periods with particularly intense (an increase in the DCF above 0.001 per sol) net dust removal. In contrast, the remaining distributions are similar, and net dust accumulation clearly dominates. Given that the ratio of net dust accumulation to net dust removal is approximately 2:1 (2,563 negative variations vs. 1,389 positive changes), the fact that these two medians are positive is particularly relevant, allowing to establish a wind stress threshold for net dust removal at around 0.014 N/m^2. In the case of DDA, only the last distribution is markedly different with most of the values (the lower limit of the box is above 0) corresponding to dust removal. The distribution for DDA > 0.7 also shows several values that correspond to moderate (dDCF/dt > $5{\cdot}10^{-4}$ sol^{-1}) and intense net dust removal periods, suggesting that the threshold for net dust removal based on the DDA is expected to be between 0.7 and 0.76. Note that the largest increases for which the DDA threshold is not reached meet the criterium of the wind stress threshold.

From Figure 8, we conclude that net dust removal (and hence, dust lifting) is favored when the wind stress or dust devil activity exceeds a given threshold. We will now further investigate net dust removal thresholds. We will analyze the predictive skill using different variables (simulated wind stress and DDA, and observed pressure drop frequency) and thresholds. This skill is quantified by means of a score that represents the fraction of the variability

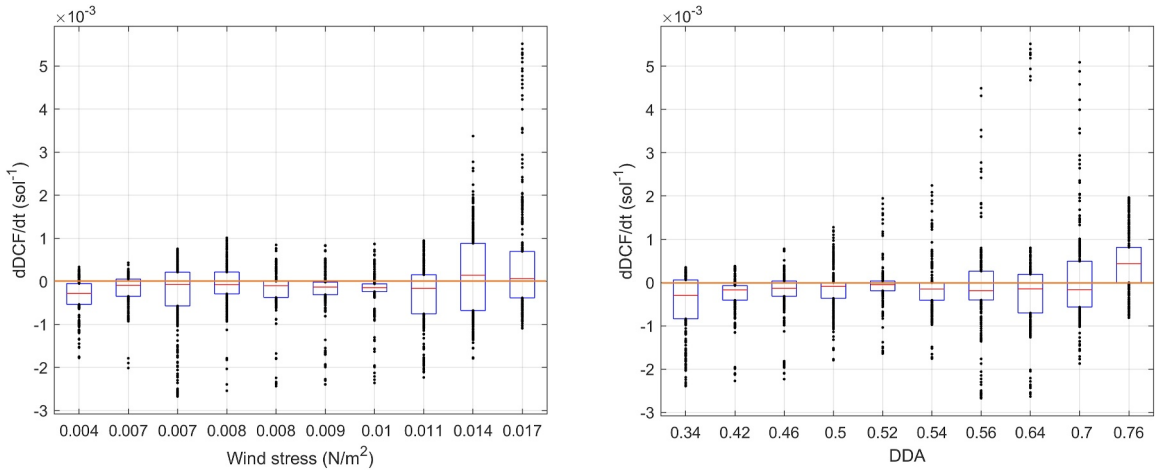


Figure 8. Boxplot showing the time rate of DCF change as a function of the daily maxima of wind stress (left) and DDA (right). The orange line separates net dust removal from net dust accumulation.

of the DCF that is correctly predicted by the model (a perfect model will present a value of 1, and a model that correctly predicts 60% of the behavior will present a value of 0.6).

The predictive skill of the models using wind stress and dust devil activity is represented in panels (a) and (b) of Figure 9, respectively. Focusing on the wind stress, the predictive skill of the model using solely this variable increases as the threshold increases until a value of 0.0161 N/m^2 is acquired. For that optimal threshold, more than 77% of the behavior is predicted correctly. A good performance (indicated by scores above 0.7) is achieved for thresholds between 0.011 and 0.017 N/m^2. A model based only on DDA would perform slightly worse than only on wind stress, reaching a maximum score for a threshold of 0.72, for which the model correctly predicts 74% of the DCF variability. Good performance was achieved for thresholds between 0.66 and 0.76. Panel f shows the

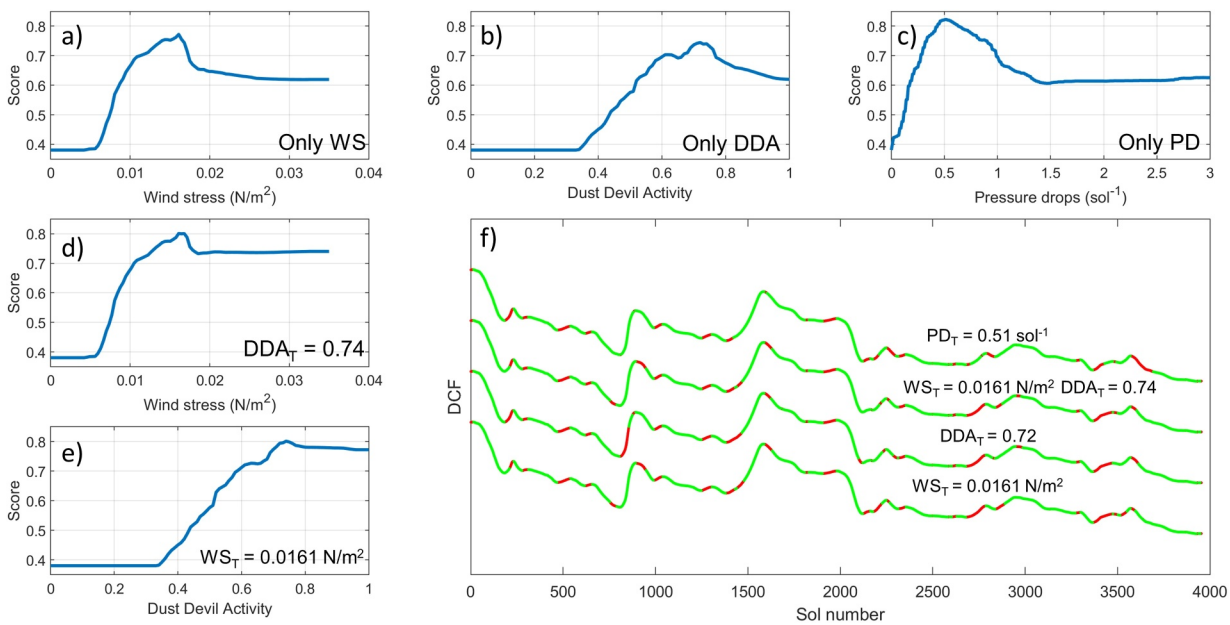


Figure 9. Predictive skill as a function of the threshold value for different input variables: (a) simulated wind stress; (b) simulated DDA; (c) observed pressure drop frequency; (d) simulated wind stress and DDA, assuming a fixed DDA threshold of 0.74; (e) as (d), but assuming a fixed wind stress threshold of 0.0161 N/m^2. Panel (f) shows the DCF four times, highlighting in green the periods when the models correctly predict the observed behavior; from bottom to top, the models assume: (i) wind stress threshold of 0.0161 N/m^2 (from panel a); (ii) DDA threshold of 0.72 (from panel b); (iii) wind stress threshold of 0.0161 N/m^2 or DDA threshold of 0.74 (from panels d and e); (iv) pressure drop frequency threshold of 0.51 drops/sol.

DCF, highlighting in green the behavior that is correctly predicted by the model. When comparing the models using only wind stress or dust devil activity, results are very similar, except during most of the intense dust removal event around sol 850, when the model based on DDA shows a lack of predictive skill.

In panels (d) and (e) we further analyze the predictive skill of the model, but now consider both variables and assume that net dust removal occurs when any of the two thresholds is reached. The highest skill was obtained for a wind stress threshold of 0.0161 N/m^2 (the same value as when using only wind stress) and for a DDA threshold of 0.74 (slightly larger than before). In these panels, we only change one of the thresholds, and the fixed threshold is set to one of the aforementioned values. When both variables are used, the predictive skill of the model increases, predicting correctly slightly above 80% of the DCF behavior for that combination of thresholds.

Figure 9 also allows us to compare the predictive skill of the model that combines simulated values of wind stress and DDA to that of a model that relies on a pressure drop frequency threshold. Figure 9c shows the predictive skill as a function of the pressure drop frequency threshold, obtaining that the optimal threshold is obtained for 0.51 drops/sol detected during the first 5 min of each hour, which is consistent with the value anticipated from Figure 5. For this optimal threshold, the model correctly predicts more than 82% of the observed DCF behavior. Compared to the model that uses both simulated wind stress and DDA (Figure 9f), the observed pressure drop frequency presents a higher predictive skill mainly during the net dust removal periods of MY 34 to 36, and a lower skill after the DCF maximum in MY 36 (sols 3,600–3,700). In summary, models based either on wind stress or DDA thresholds show a high predictive skill, which further increases when both variables are considered; similar predictive skill is achieved using MarsWRF simulations or observed pressure drop frequency, validating the use of MarsWRF to establish dust lifting thresholds.

From Figure 9, we conclude that both wind stress and dust devil activity can be used to predict the behavior of the DCF. In order to better understand the potential relative roles of convective vortices and wind stress, we assess the periods of high DDA or high wind stress, defined as those for which the thresholds exceed 0.0161 N/m^2 and 0.74, respectively. Figure 10 shows the DCF (black), highlighting the periods with high wind stress (blue), high DDA (green), and the periods when both DDA and wind stress are high (red). The strongest net dust removal event occurred in MY 33 (sols 1,400–1,600) when both wind stress (mainly around 18H) and dust devil activity were particularly high (Figures 6 and 7). The combined effect of these strong winds and numerous convective vortices, added to the proximity of the rover to Bagnold Dunes, a region with active sand motion and frequent dust lifting (Guzewich et al., 2023), appear to be the cause of the annual net cleaning of the sensor during MY 33, as evidenced in the images of Figure 2. During the strong net dust removal period of MY 32 (sols 800–900), only wind stress was particularly high. In addition, the beginning of the period of weak net dust removal in MY 31 coincides with a period of strong winds. Hence, it appears that strong turbulent winds are the main dust removal mechanism in MY 31 and 32.

In contrast, during MY 34 and 36, the net dust removal periods are better captured by high values of dust devil activity; this is particularly notorious in MY 34, when the strong decreasing trend in the DCF caused by the Global Dust Storm is reverted when the DDA exceeds the proposed threshold, and wind stress exceeds the threshold only around the annual minimum in accumulated dust, with virtually no net variation in the DCF. This suggests that the rover transitioned from a region where dust devil activity was relatively low but where local topography caused strong turbulent winds (MY 31 and 32) to a region where dust devils became more frequent and increased their relative contribution to dust lifting; this is consistent with Navcam observations of dust lifting events: 79% of the dust lifting events between the perihelion season of MY 33 and the aphelion season of MY 37 were attributed to dust devils and 16% to linear wind stress (Guzewich et al., 2023).

Our dust removal threshold for wind stresses between 0.011 and 0.017 N/m^2 is consistent with the effective threshold for sand motion of 0.010 N/m^2 derived by Ayoub et al. (2014). Our value should be interpreted as a first approximation of an effective value throughout the mission. It is expected that the threshold could be lower in the proximity to sand dunes (dust lifting through sand saltation requires lower thresholds that direct dust injection into the atmosphere), and larger in regions far from them. During the strongest net dust removal period, surface thermal inertia was particularly low (Martinez et al., 2021), suggesting the presence of loose material that could favor dust lifting. In addition, net dust removal requires the effect of dust deposition to be smaller than that of the dust removal. Dust deposition is expected to be larger during periods where there are large amounts of suspended dust that can be potentially deposited on the surface, and conditions for net dust removal are less restrictive when the deposition rates are low. For these reasons, net dust removal thresholds are expected to depend on location and

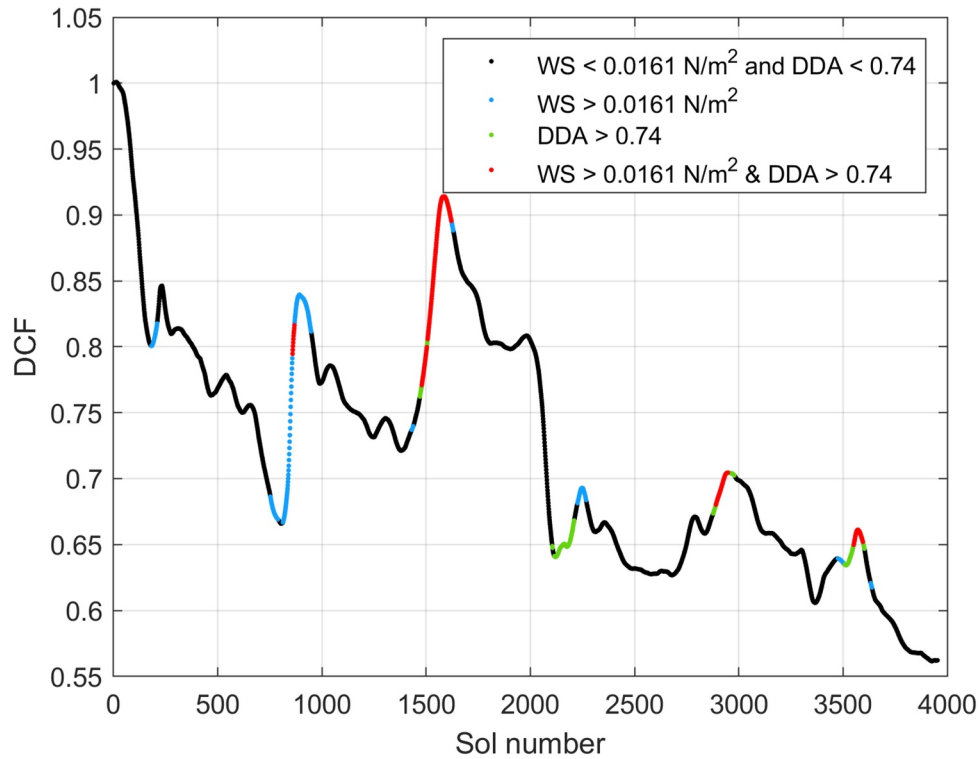


Figure 10. Comparison of dust accumulation and removal with periods in which wind stress or DDA exceed the thresholds derived from Figure 9. Periods when both thresholds are shown in red; those when only wind stress or only dust devil activity thresholds are exceeded are shown in blue and green, respectively; periods in which none of the thresholds are exceeded are shown in black.

time of the year. However, it is noteworthy that the use of constant thresholds provides a high predictive skill, predicting correctly slightly more than 80% of the DCF behavior.

4.2. Comparison With ChemCam Observations

In this section, we complement the previous analysis of the dust accumulated on the photodiode windows of the REMS UV sensor by analyzing retrievals of the 535 nm band depth (associated with the presence of ferric materials, a component of Martian dust) on the Target #11 (target holder with white paint coating, shown in Figure 1) of the ChemCam Calibration Target (CCCT).

Figure 11 compares the proxies of dust cover on the two types of surfaces. The blue line represents the average DCF on the photodiode windows of the REMS UVS and the orange connected dots represent the complement of the 535 nm band depth (535BD) on the Target #11 of the CCCT. In general, both surfaces follow the same temporal evolution of dust accumulation. Both surfaces underwent a period of significant dust accumulation during the first 700–800 sols of the mission. Then, the strong net dust removal period detected by the REMS UVS during the MY 32 perihelion season was also observed on the CCCT. Between sols 900 and 1,400, both surfaces experienced net dust accumulation, which was followed by a strong net dust removal period centered around sol 1,500. After the MY 34 Global Dust Storm, both surfaces showed coincident annual minima in dust accumulation (maxima in the proxies) for MY 34 (sol ~ 2,300), MY 35 (sol ~ 2,950), and MY 36 (sol ~ 3,600). The similarities between both surfaces are noteworthy, particularly considering the differences among them: the CCCT is a tilted surface and the REMS photodiode windows are surrounded by magnetic rings. Hence, from this comparison, we have addressed the robustness of the seasonal cycle of dust deposition and removal, concluding that the presented results are representative of the corresponding cycle on surfaces with different properties.

However, there are also some differences. The most remarkable difference is that, while both curves virtually coincide during the first 2,000 sols, there is a significant offset after sol 2,200. We analyze in greater detail what happened between sols 1,944 and 2,230 when the last/first retrievals of the 535 band depth on the CCCT prior to/

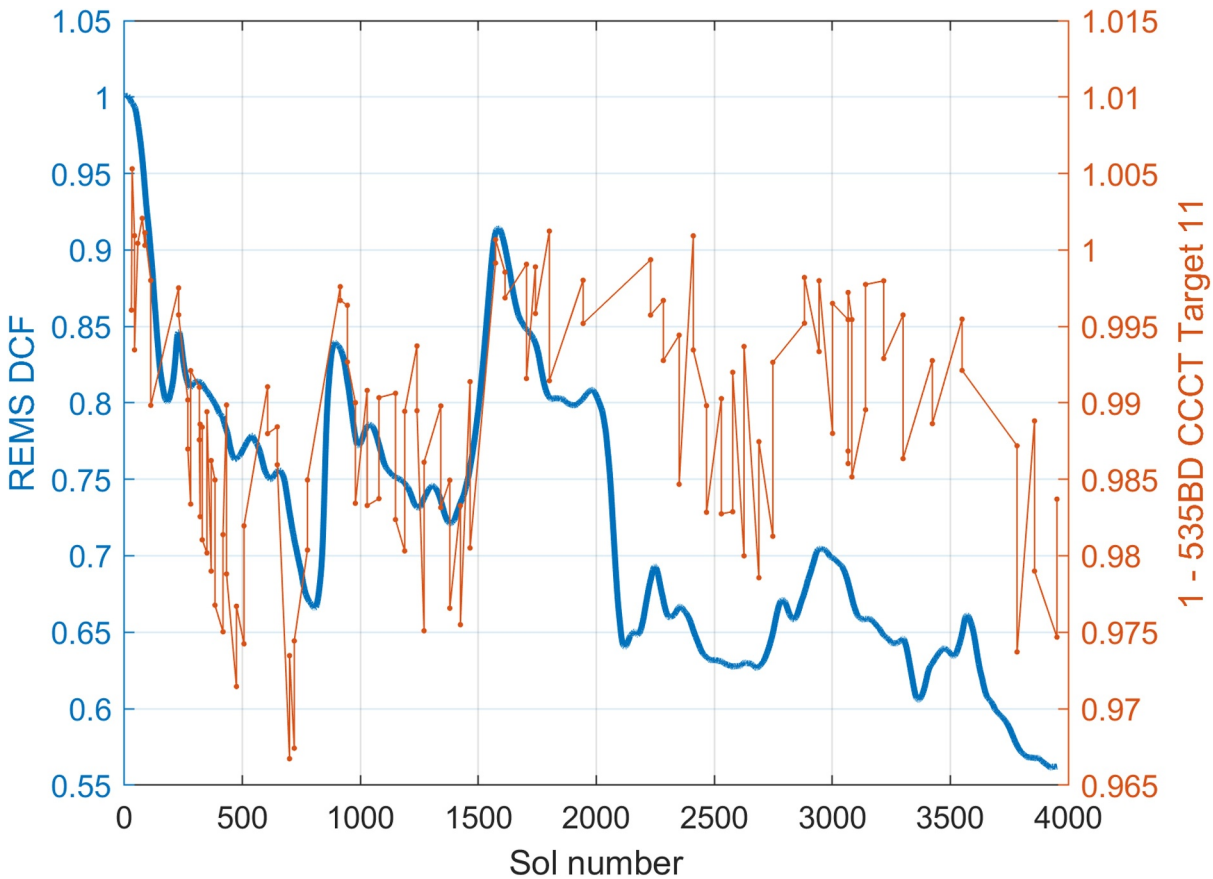


Figure 11. Comparison of the dust cover proxies on the two types of surfaces: The REMS photodiode windows (characterized with the DCF, blue) and Target #11 (white paint) of the ChemCam Calibration Target (characterized with 1–535BD, orange).

after the global dust storm were obtained. The REMS DCF shows an extraordinarily strong decrease in value between until sol ~ 2,120, followed by a moderate increase until sol 2,250. The effect of dust deposition on the REMS UVS clearly dominated over the effect of any dust lifting mechanism during the period of the highest opacities. The transition between net dust accumulation and removal coincided with the time in which the decrease in dust opacity crossed the threshold of $\tau = 4$. Then, even though the opacity remained higher than the typical annual maxima in the absence of global dust storms, dust removal had a larger effect than dust deposition during this part of the storm decay phase when opacity decreased from 4 to values below 1.

The net effect of the Global Dust Storm was a significant increase in dust accumulation on the REMS UVS between sols 1,944 and 2,230. In contrast, the complement of the 535 nm band depth showed a slight increase between these two sols, indicating a slight decrease in dust cover on Target #11 of the CCCT. Images of the vertically mounted MAHLI calibration target showed a significant increase in dust cover between sols 2,082 and 2,161, and an extraordinary decrease between sols 2,161 and 2,248, when the target presented less dust coverage than at the beginning of the mission (Yingst et al., 2020). The lack of measurements on the CCCT does not allow us to know whether this surface also presented a local maximum in dust cover immediately after the most intense period of the storm; however, the net effect is consistent with REMS and MAHLI observations, being between the strong dust accumulation on the horizontal sensor and the virtually total cleaning of the vertical calibration target. This suggests that the effect of surface tilt could be particularly remarkable around the occurrence of intense dust storms.

5. Conclusions

In this study, we analyzed the temporal evolution of dust accumulation on the REMS UV Sensor (UVS) and on the ChemCam calibration target (CCCT) during the first 3,953 sols (more than 11 Earth years) of the Mars

Science Laboratory mission. The combined analysis of the Dust Correction Factor (DCF), together with environmental observations of atmospheric dust opacity and pressure drop frequency, and with mesoscale simulations of dust devil activity and wind stress, improve our understanding of dust lifting processes on Mars. The main findings are:

After six Mars Years, dust accumulated on the REMS UVS attenuates around 45% of the incoming radiation, highlighting the suitability of the Gale Crater for long-term solar-powered missions. The DCF follows the same temporal evolution for the six REM UV channels, suggesting that trends are robust. There are some quantitative differences among channels (attenuation is below 40% and above 50% at the end of the analyzed period for the UVA and UVC channels, respectively), which could be a combination of spatial variability and a wavelength-dependent effect of the accumulated dust.

The DCF follows a seasonal cycle, with gradual net dust accumulation during the aphelion season, followed by a period of net dust removal, reaching a maximum (representing minimum dust accumulation) at Ls ∼300°. There is a significant interannual variability attributed to variability in dust removal mechanisms and to the intensity of dust storms; hence, some years present annual net dust accumulation and others annual net dust removal. Dust removal periods align with those of observed high pressure drop frequency. The strongest net dust removal periods occur in MY 32 and 33, and are significantly stronger than in other years. The strongest net dust accumulation periods occurred in MY 34 due to the Global Dust Storm and at the beginning of the mission due to the combination of low dust lifting activity, relatively high atmospheric opacity and virtual absence of previous dust accumulation.

We have presented and analyzed wind stress and Dust Devil Activity at the rover location every 3 hr throughout the mission using simulations of the MarsWRF mesoscale model. DDA follows a marked seasonal cycle, with a maximum around Ls ∼ 300°, and moderate interannual variability, being maximum in MY 33 and minimum in MY 31. Wind stress presents high intrasol, seasonal and interannual variability. In general, values are higher during the perihelion season, but this seasonal cycle is clearer during the night. Maximum values are found at 18H during the perihelion season of MY 32 and 33, coinciding with the strongest dust removal periods. Dust lifting mechanisms are variable, with a larger relative importance of wind stress in MY 31 and 32, and of dust devils in MY 34 to 36. The significant annual net dust removal of MY 33 is the combination of strong winds and high dust devil activity. Models based either on wind stress or DDA thresholds show a high predictive skill, which further increases when both variables are considered; more than 80% of the DCF behavior can be predicted correctly considering that net dust removal occurs when either a wind stress threshold of 0.0161 N/m^2 or a DDA threshold of 0.74 are reached.

We have compared dust accumulation on the REMS UVS with that on Target #11 of the ChemCam Calibration Target. Despite the differences between both surfaces (the REMS UV sensor is mounted horizontally and there are magnets surrounding the analyzed surfaces, while the CCCT surface is strongly tilted and is not affected by magnets), both dust cover proxies follow the same trends. However, the 2018 Global Dust Storm caused a marked offset between both surfaces: the REMS UV sensor suffered significant dust accumulation, while the CCCT experienced a light net dust removal. This suggests that the effect of surface tilt becomes particularly important during periods of intense dust storms.

Data Availability Statement

REMS photocurrents (TELRDR products, Gomez-Elvira, 2013a) and ancillary data (ADR products, Gomez-Elvira, 2013b) used in this work are stored in the NASA Planetary Data System (PDS) Atmospheres node (https://atmos.nmsu.edu/data_and_services/atmospheres_data/MARS/curiosity/rems.html). Mastcam images (Malin, 2013) are available in the NASA PDS Cartography and Imaging Sciences node (https://pds-imaging.jpl.nasa.gov/volumes/msl.html). Atmospheric dust opacity measurements (Lemmon et al., 2024b) are available in the NASA PDS Atmospheres node (https://pds-atmospheres.nmsu.edu/data_and_services/atmospheres_data/MARS/curiosity/atmospheric_opacity.html). Data derived from this work are publicly available in Vicente-Retortillo (2025).

Acknowledgments
This research was funded by the Spanish Ministry of Science and Innovation (MCIN)/State Agency of Research (AEI) project PID2021-126719OB-C41, funded by MCIN/AEI/10.13039/501100011033/ FEDER, UE. J.R. J. is funded through the MSL Participating Scientist Program (80NSSC22K0779). Mastcam mosaics were processed by the Mastcam team at Malin Space Science Systems. We are thankful to the MSL team for the efforts to support this work.

References

Ayoub, F., Avouac, J. P., Newman, C., Richardson, M., Lucas, A., Leprince, S., & Bridges, N. (2014). Threshold for sand mobility on Mars calibrated from seasonal variations of sand flux. *Nature Communications*, *5*(1), 5096. https://doi.org/10.1038/ncomms6096

Basu, S., Richardson, M. I., & Wilson, R. J. (2004). Simulation of the Martian dust cycle with the GFDL Mars GCM. *Journal of Geophysical Research*, *109*(E11), E11006. https://doi.org/10.1029/2004je002243

Bell, J. F., III, Godber, A., McNair, S., Caplinger, M. A., Maki, J. N., Lemmon, M. T., et al. (2017). The Mars Science Laboratory *Curiosity* rover Mastcam instruments: Preflight and in-flight calibration, validation, and data archiving. *Earth and Space Science*, *4*(7), 396–452. https://doi.org/10.1002/2016EA000219

Crisp, D., Pathare, A., & Ewell, R. C. (2004). The performance of gallium arsenide/germanium solar cells at the Martian surface. *Acta Astronautica*, *54*(2), 83–101. https://doi.org/10.1016/s0094-5765(02)00287-4

Drube, L., Leer, K., Goetz, W., Gunnlaugsson, H. P., Haspang, M. P., Lauritsen, N., et al. (2010). Magnetic and optical properties of airborne dust and settling rates of dust at the Phoenix landing site. *Journal of Geophysical Research*, *115*(E5), E00E23. https://doi.org/10.1029/2009JE003419

Ellehoj, M. D., Gunnlaugsson, H. P., Taylor, P. A., Kahanpää, H., Bean, K. M., Cantor, B. A., et al. (2010). Convective vortices and dust devils at the Phoenix Mars mission landing site. *Journal of Geophysical Research*, *115*(E4), E00E16. https://doi.org/10.1029/2009JE003413

Garratt, J. R. (1994). The atmospheric boundary layer. *Earth-Science Reviews*, *37*(1–2), 89–134. https://doi.org/10.1016/0012-8252(94)90026-4

Gomez-Elvira, J. (2013a). Mars science laboratory rover environmental monitoring station RDR data V1.0, MSL-M-REMS-3-TELEDR-V1.0 [Dataset]. *NASA Planetary Data System*. https://doi.org/10.17189/gvf7-4358

Gomez-Elvira, J. (2013b). Mars science laboratory rover environmental monitoring station RDR data V1.0, MSL-M-REMS-6-ADR-V1.0 [Dataset]. *NASA Planetary Data System*. https://doi.org/10.17189/yjdt-2f87

Gómez-Elvira, J., Armiens, C., Carrasco, I., Genzer, M., Gómez, F., Haberle, R., et al. (2014). Curiosity's rover environmental monitoring station: Overview of the first 100 sols. *Journal of Geophysical Research: Planets*, *119*(7), 1680–1688. https://doi.org/10.1002/2013JE004576

Gómez-Elvira, J., Armiens, C., Castañer, L., Domínguez, M., Genzer, M., Gómez, F., et al. (2012). REMS: The environmental sensor suite for the Mars science laboratory rover. *Space Science Reviews*, *170*(1–4), 583–640. https://doi.org/10.1007/s11214-012-9921-1

Grotzinger, J. P., Crisp, J., Vasavada, A. R., Anderson, R. C., Baker, C. J., Barry, R., et al. (2012). Mars science laboratory mission and science investigation. *Space Science Reviews*, *170*(1–4), 5–56. https://doi.org/10.1007/s11214-012-9892-2

Guzewich, S. D., Lemmon, M., Smith, C. L., Martínez, G., de Vicente-Retortillo, Á., Newman, C. E., et al. (2019). Mars science laboratory observations of the 2018/Mars year 34 global dust storm. *Geophysical Research Letters*, *46*(1), 71–79. https://doi.org/10.1029/2018GL080839

Guzewich, S. D., Mason, E. L., Lemmon, M. T., Newman, C. E., & Lewis, K. W. (2023). Dust lifting observations with the Mars Science Laboratory navigation cameras. *Journal of Geophysical Research: Planets*, *128*(10), e2023JE007959. https://doi.org/10.1029/2023JE007959

Harri, A.-M., Genzer, M., Kemppinen, O., Kahanpää, H., Gomez-Elvira, J., Rodriguez-Manfredi, J. A., et al. (2014). Pressure observations by the Curiosity rover: Initial results. *Journal of Geophysical Research: Planets*, *119*(1), 82–92. https://doi.org/10.1002/2013JE004423

Johnson, J. R., Bell III, J. F., Bender, S., Blaney, D., Cloutis, E., DeFlores, L., et al. (2015). ChemCam passive reflectance spectroscopy of surface materials at the Curiosity landing site, Mars. *Icarus*, *249*, 74–92. https://doi.org/10.1016/j.icarus.2014.02.028

Kahanpää, H., Newman, C., Moores, J., Zorzano, M., Martín-Torres, J., Navarro, S., et al. (2016). Convective vortices and dust devils at the MSL landing site: Annual variability. *Journal of Geophysical Research: Planets*, *121*(8), 1514–1549. https://doi.org/10.1002/2016JE005027

Kahre, M. A., Murphy, J. R., & Haberle, R. M. (2006). Modeling the Martian dust cycle and surface dust reservoirs with the NASA Ames general circulation model. *Journal of Geophysical Research*, *111*(E6), E06008. https://doi.org/10.1029/2005je002588

Kahre, M. A., Murphy, J. R., Newman, C. E., Wilson, R. J., Cantor, B. A., Lemmon, M. T., & Wolff, M. J. (2017). The Mars dust cycle. In R. Haberle, R. T. Clancy, F. Forget, M. D. Smith, & R. W. Zurek (Eds.), *The atmosphere and climate of Mars* (pp. 295–337). Cambridge Univ. Press.

Kass, D. M., Kleinböhl, A., McCleese, D. J., Schofield, J. T., & Smith, M. D. (2016). Interannual similarity in the Martian atmosphere during the dust storm season. *Geophysical Research Letters*, *43*, 6111–6118. https://doi.org/10.1002/2016GL068978

Lemmon, M. T., Guzewich, S., Battalio, J., Malin, M., Vicente-Retortillo, A., Zorzano, M. P., et al. (2024b). The Mars science laboratory record of optical depth measurements via solar imaging [Dataset]. *NASA Planetary Data System*, *408*. 115821. https://doi.org/10.17189/fjh0-2978

Lemmon, M. T., Guzewich, S. D., Battalio, J. M., Malin, M. C., Vicente-Retortillo, A., Zorzano, M. P., et al. (2024a). The Mars Science Laboratory record of optical depth measurements via solar imaging. *Icarus*, *408*, 115821. https://doi.org/10.1016/j.icarus.2023.115821

Lemmon, M. T., Newman, C. E., Rennon, N., Mason, E., Battalio, M., Richardson, M. I., & Kahanpää, H. (2017). Dust devil activity at the curiosity Mars rover field site. In *Presented at the 48th lunar and planetary science conference* (p. 2952).

Lorenz, R. D., Martínez, G. M., Spiga, A., Vicente-Retortillo, A., Newman, C. E., Murdoch, N., et al. (2021). Lander and rover histories of dust accumulation on and removal from solar arrays on Mars. *Planetary and Space Science*, *207*, 105337. https://doi.org/10.1016/j.pss.2021.105337

Madsen, M. B., Bertelsen, P., Goetz, W., Binau, C. S., Olsen, M., Folkmann, F., et al. (2003). Magnetic properties experiments on the mars exploration rover mission. *Journal of Geophysical Research*, *108*(E12), 8069. https://doi.org/10.1029/2002JE002029

Malin, M. (2013). *MSL Mars mast camera RDR V1.0*. NASA Planetary Data System. Retrieved from https://pds-imaging.jpl.nasa.gov/volumes/msl.html

Martínez, G. M., Newman, C. N., De Vicente-Retortillo, A., Fischer, E., Renno, N. O., Richardson, M. I., et al. (2017). The modern near-surface Martian climate: A review of in-situ meteorological data from Viking to curiosity. *Space Science Reviews*, *212*(1–2), 295–338. https://doi.org/10.1007/s11214-017-0360-x

Martínez, G. M., Vicente-Retortillo, A., Vasavada, A. R., Newman, C. E., Fischer, E., Rennó, N. O., et al. (2021). The surface energy budget at Gale crater during the first 2500 sols of the Mars Science Laboratory mission. *Journal of Geophysical Research: Planets*, *126*(9), e2020JE006804. https://doi.org/10.1029/2020JE006804

Martín-Rubio, C., Vicente-Retortillo, A., Gómez, F., & Rodríguez-Manfredi, J. A. (2024). Interannual variability of regional dust storms between Mars years 24 and 36. *Icarus*, *412*, 115982. https://doi.org/10.1016/j.icarus.2024.115982

Martín-Rubio, C., Vicente-Retortillo, A., Martínez-Esteve, G., Gómez, F., & Rodríguez-Manfredi, J. A. (2024). Global characterization of the early-season dust storm of Mars year 36. *Icarus*, 116369. https://doi.org/10.1016/j.icarus.2024.116369

MEPAG MCE-SAG Final Report. (2023). Mars concurrent exploration science analysis group (MCE-SAG). In M. Mischna & B. Horgan (Eds.), *Posted on 18 July 2023 by the Mars exploration program analysis group* (p. 94). Retrieved from https://www.lpi.usra.edu/mepag/reports/reports/MCE_SAG_Final_Report.pdf

Michaels, T. I. (2006). Numerical modeling of Mars dust devils: Albedo track generation. *Geophysical Research Letters*, *33*(19), L19S08. https://doi.org/10.1029/2006GL026268

Morris, R. V., Golden, D. C., Bell, J. F., III., Shelfer, T. D., Scheinost, A. C., Hinman, N. W., et al. (2000). Mineralogy, composition, and alteration of Mars Pathfinder rocks and soils: Evidence from multispectral, elemental, and magnetic data on terrestrial analogue, SNC meteorite, and Pathfinder samples. *Journal of Geophysical Research*, *105*(E1), 1757–1817. https://doi.org/10.1029/1999je001059

Newman, C. E., Gómez-Elvira, J., Marin, M., Navarro, S., Torres, J., Richardson, M. I., et al. (2017). Winds measured by the rover environmental monitoring station (REMS) during the Mars science laboratory (MSL) rover's Bagnold dunes Campaign and comparison with numerical modeling using MarsWRF. *Icarus*, *291*, 203–231. https://doi.org/10.1016/j.icarus.2016.12.016

Newman, C. E., Kahanpää, H., Richardson, M. I., Martinez, G. M., Vicente-Retortillo, A., & Lemmon, M. (2019). Convective vortex and dust devil predictions for gale crater over 3 mars years and comparison with MSL-REMS observations. *Journal of Geophysical Research: Planets*, *124*, 3442–3468. https://doi.org/10.1029/2019JE006082

Newman, C. E., Lewis, S. R., Read, P. L., & Forget, F. (2002a). Modeling the Martian dust cycle, 1. Multiannual radiatively active dust transport simulations. *Journal of Geophysical Research*, *107*(E12), 6-1–6-18. https://doi.org/10.1029/2002je001910

Newman, C. E., Lewis, S. R., Read, P. L., & Forget, F. (2002b). Modeling the Martian dust cycle 2. Multiannual radiatively active dust transport simulations. *Journal of Geophysical Research*, *107*(E12), 7-1–7-15. https://doi.org/10.1029/2002je001920

Ordonez-Etxeberria, I., Hueso, R., & Sánchez-Lavega, A. (2018). A systematic search of sudden pressure drops on Gale crater during two Martian years derived from MSL/REMS data. *Icarus*, *299*, 308–330. https://doi.org/10.1016/j.icarus.2017.07.032

Pla-Garcia, J., Rafkin, S. C., Kahre, M., Gomez-Elvira, J., Hamilton, V. E., Navarro, S., et al. (2016). The meteorology of Gale crater as determined from rover environmental monitoring station observations and numerical modeling. Part I: Comparison of model simulations with observations. *Icarus*, *280*, 103–113. https://doi.org/10.1016/j.icarus.2016.03.013

Rafkin, S. C., Haberle, R. M., & Michaels, T. I. (2001). The Mars regional atmospheric modeling system: Model description and selected simulations. *Icarus*, *151*(2), 228–256. https://doi.org/10.1006/icar.2001.6605

Rafkin, S. C. R., Pla-Garcia, J., Kahre, M., Gomez-Elvira, J., Hamilton, V. E., Marín, M., et al. (2016). The meteorology of Gale Crater as determined from Rover Environmental Monitoring Station observations and numerical modeling. Part II: Interpretation. *Icarus*, *280*, 114–138. https://doi.org/10.1016/j.icarus.2016.01.031

Rennó, N. O., Burkett, M. L., & Larkin, M. P. (1998). A simple thermodynamical theory for dust devils. *Journal of the Atmospheric Sciences*, *55*(21), 3244–3252. https://doi.org/10.1175/1520-0469(1998)055<3244:asttfd>2.0.co;2

Rice, M. S., Seeger, C., Bell, J., Calef, F., St. Clair, M., Eng, A., et al. (2022). Spectral diversity of rocks and soils in Mastcam observations along the Curiosity rover's traverse in Gale crater, Mars. *Journal of Geophysical Research: Planets*, *127*(8), e2021JE007134. https://doi.org/10.1029/2021je007134

Richardson, M. I., Toigo, A. D., & Newman, C. E. (2007). PlanetWRF: A general purpose, local to global numerical model for planetary atmospheric and climate dynamics. *Journal of Geophysical Research*, *112*(E9), E09001. https://doi.org/10.1029/2006JE002825

Smith, M. D., Zorzano, M.-P., Lemmon, M., Martín-Torres, J., & Mendaza de Cal, T. (2016). Aerosol optical depth as observed by the Mars Science Laboratory REMS UV photodiodes. *Icarus*, *280*, 234–248. https://doi.org/10.1016/j.icarus.2016.07.012

Spiga, A., Faure, J., Madeleine, J.-B., Määttänen, A., & Forget, F. (2013). Rocket dust storms and detached dust layers in the Martian atmosphere. *Journal of Geophysical Research: Planets*, *118*(4), 746–767. https://doi.org/10.1002/jgre.20046

Spiga, A., & Forget, F. (2009). A new model to simulate the Martian mesoscale and microscale atmospheric circulation: Validation and first results. *Journal of Geophysical Research*, *114*(E2), E02009. https://doi.org/10.1029/2008JE003242

Spiga, A., Murdoch, N., Lorenz, R., Forget, F., Newman, C., Rodriguez, S., et al. (2021). A study of daytime convective vortices and turbulence in the Martian planetary boundary layer based on half-a-year of InSight atmospheric measurements and large-eddy simulations. *Journal of Geophysical Research: Planets*, *126*(1), e2020JE006511. https://doi.org/10.1029/2020JE006511

Steakley, K., & Murphy, J. (2016). A year of convective vortex activity at Gale crater. *Icarus*, *278*, 180–193. https://doi.org/10.1016/j.icarus.2016.06.010

Stella, P. M., & Herman, J. A. (2010). The Mars surface environment and solar array performance. In *Photovoltaic specialists conference (PVSC), 2010 35th IEEE* (pp. 002631–002635).

Vicente-Retortillo, A. (2025). Derived data supporting the analysis of dust lifting and deposition over six Mars Years at Gale crater, Mars [Dataset]. *Zenodo*. https://doi.org/10.5281/zenodo.15056579

Vicente-Retortillo, A., Lemmon, M. T., Martinez, G. M., Toledo, D., Apéstigue, V., Arruego, I., et al. (2024). Dust accumulation and lifting at the landing site of the Mars 2020 mission, Jezero crater, as observed from MEDA. *Geophysical Research Letters*, *51*(11), e2023GL107975. https://doi.org/10.1029/2023GL107975

Vicente-Retortillo, Á., Martínez, G. M., Rennó, N., Newman, C. E., Ordonez-Etxeberria, I., Lemmon, M. T., et al. (2018). Seasonal deposition and lifting of dust on Mars as observed by the Curiosity rover. *Scientific Reports*, *8*(1), 17576. https://doi.org/10.1038/s41598-018-35946-8

Vicente-Retortillo, Á., Martínez, G. M., Renno, N. O., Lemmon, M. T., & de la Torre-Juárez, M. (2017). Determination of dust aerosol particle size at Gale Crater using REMS UVS and Mastcam measurements. *Geophysical Research Letters*, *44*(8), 3502–3508. https://doi.org/10.1002/2017GL072589

Vicente-Retortillo, A., Martínez, G. M., Rennó, N. O., Lemmon, M. T., de la Torre-Juárez, M., & Gómez-Elvira, J. (2020). In situ UV Measurements by MSL/REMS: Dust deposition and angular response corrections. *Space Science Reviews*, *216*(5), 97. https://doi.org/10.1007/s11214-020-00722-6

Vicente-Retortillo, Á., Valero, F., Vázquez, L., & Martínez, G. M. (2015). A model to calculate solar radiation fluxes on the Martian surface. *Journal of Space Weather and Space Climate*, *5*, A33. https://doi.org/10.1051/swsc/2015035

Viúdez-Moreiras, D., Gómez-Elvira, J., Newman, C. E., Navarro, S., Marin, M., Torres, J., & De La Torre-Juárez, M. (2019). Gale surface wind characterization based on the Mars Science Laboratory REMS dataset. Part I: Wind retrieval and Gale's wind speeds and directions. *Icarus*, *319*, 909–925. https://doi.org/10.1016/j.icarus.2018.10.011

Wiens, R. C., Maurice, S., Barraclough, B., Saccoccio, M., Barkley, W. C., Bell, J. F., III, et al. (2012). The ChemCam instrument suite on the Mars science laboratory (MSL) rover: Body unit and combined system tests. *Space Science Reviews*, *170*(1–4), 167–227. https://doi.org/10.1007/s11214-012-9902-4

Yingst, R. A., Bray, S., Herkenhoff, K., Lemmon, M., Minitti, M. E., Schmidt, M., et al. (2020). Dust cover on curiosity′s Mars hand lens imager (MAHLI) calibration target: Implications for deposition and removal mechanisms. *Icarus*, *351*, 113872. https://doi.org/10.1016/j.icarus.2020.113